Robustness of longitudinal transmon readout to ionization

Alex A. Chapple, 1,* Alexander McDonald, 1 Manuel H. Muñoz-Arias, 1,† Mathieu Lachapelle, 1,‡ and Alexandre Blais 1,2

¹Institut Quantique and Département de Physique, Université de Sherbrooke, Sherbrooke J1K 2R1, Quebec, Canada

²CIFAR, Toronto, Ontario M5G 1M1, Canada

(Received 1 March 2025; revised 8 April 2025; accepted 6 August 2025; published 9 September 2025)

Multiphoton processes deteriorate the quantum nondemolition (QND) character of the dispersive readout in circuit QED, causing the readout to lag behind single- and two-qubit gates in both speed and fidelity. Alternative methods such as longitudinal readout have been proposed; however, it is unknown to what extent multiphoton processes hinder this approach. Here, we investigate the QND character of the longitudinal readout of the transmon qubit. We show that the deleterious effects that arise due to multiphoton transitions can be heavily suppressed with detuning because the longitudinal interaction strength is independent of the transmon-resonator detuning. We consider the effect of circuit disorder, the selection rules that act on the transmon, and the description of longitudinal readout in the classical limit of the transmon to qualitatively demonstrate that longitudinal readout is robust. We show that fast, high-fidelity OND readout of transmon qubits is possible with longitudinal coupling.

DOI: 10.1103/mp2x-zj3y

I. INTRODUCTION

Fast and high-fidelity quantum nondemolition (QND) qubit readout is essential for fault-tolerant quantum computers [1]. The standard method for qubit measurement in circuit quantum electrodynamics (cQED) is the dispersive readout, in which a resonator coupled to the qubit undergoes a qubit-state-dependent frequency shift [2]. By probing this frequency shift with a measurement pulse, the qubit state can be inferred. Optimization of the dispersive readout has resulted in readout fidelity exceeding 99.9% in an integration time of less than 60 ns [3-6]. Despite this tremendous progress, readout lags behind in performance compared to other qubit operations such as single- and two-qubit gates [7-10]. An important difficulty in improving the dispersive readout is that, at short times, the response of the resonator depends only weakly on the qubit state, making it difficult to shorten the measurement time. Even more problematic is the breakdown of the QND character of this readout observed at small to moderate measurement photon numbers filling the resonator [5,11–15].

Roughly speaking, this can be traced back to the transverse nature of the qubit-resonator coupling $\hat{H}_x = g_x(\hat{a}^{\dagger} +$ \hat{a}) $\hat{\sigma}_x$ at the origin of this readout. In the dispersive regime, where the qubit-resonator frequency detuning Δ is large compared to the coupling g_x , the transverse interaction can be perturbatively reduced to $\hat{H}_{\chi} = \chi_x \hat{a}^{\dagger} \hat{a} \hat{\sigma}_z$, where $\chi_x =$ $g_{\rm r}^2/\Delta$ is the dispersive coupling. While the approximate dispersive Hamiltonian supports a QND measurement, its parent Hamiltonian \hat{H}_x does not, leading to qubit-state transitions [11,12,14,16–19]. More precisely, the root cause of the above issue is multiphoton resonances resulting in measurement-induced transitions to highly excited transmon states [11], something that has also been referred to as transmon ionization [16,17,20]. Moreover, when combined with the probe tone, the dispersive interaction \hat{H}_{χ} leads to qubit-state-conditional trajectories of the resonator in phase space that are initially nearly parallel. This results in little information gain at short times and thus a need for long integration times. In addition, to maximize the resonator pointer-state separation in the steady state, and therefore the information gain at long times, the dispersive shift must be set to $2\chi_x = \kappa$, where κ is the resonator decay rate [21]. Although this can be easily done in practice, it is yet another constraint that needs to be satisfied in experiments.

Longitudinal readout is an alternative qubitmeasurement scheme introduced to alleviate these issues [22,23]. In contrast to dispersive readout, it exploits a longitudinal qubit-resonator coupling, $\hat{H}_z = g_z(\hat{a}^{\dagger} + \hat{a})\hat{\sigma}_z$ [24–28]. Because the interaction \hat{H}_z is proportional to $\hat{\sigma}_z$,

^{*}Contact author: alex.arimoto.chapple@usherbrooke.ca

[†]Present address: Quantum Algorithms and Applications Collaboratory, Sandia National Laboratories, Livermore, California 94550, USA.

[‡]Present address: Canadian Centre for Climate Modelling and Analysis, Environment and Climate Change Canada, Victoria, British Columbia, Canada.

measurements of the qubit state are ideally QND. In addition, H_z generates the optimal displacements of the two qubit-state-dependent resonator states that are 180° out of phase, allowing for short measurement times [29]. The absence of dressing between the qubit and resonator state under the longitudinal interaction has the added advantage of avoiding Purcell decay [25,26]. Furthermore, the longitudinal interaction relaxes the matching condition $2\chi_x = \kappa$ of the dispersive readout. One approach to obtaining an effective longitudinal interaction is to strongly drive a resonator dispersively coupled to a qubit, the strong drive displacing the cavity field $\hat{a} \rightarrow \hat{a} + \alpha$ [2,30]. For large amplitudes of the cavity field α , this leads to a dominantly longitudinal interaction with $g_z = \alpha \chi$; however, if the dispersive interaction originates from a transversal interaction, this approach is not free from the limitations mentioned above.

The advantages of longitudinal readout over dispersive readout were derived under the assumption of an ideal two-level system [22]. In this work, we revisit the longitudinal readout of the transmon gubit without using this significant approximation, instead accounting for the full cosine potential of the Josephson junction. This is particularly important in light of the advances made in the understanding of the phenomenology responsible for the non-QNDness of the dispersive readout [11,12,14,16–18]. In those works, it was recognized that the loss of the QND character of the transmon is due to photon-number-specific resonances of the coupled qubit-resonator system [11], and that the impact of these resonances can only be correctly captured by considering the cosine potential of the transmon. These resonances allow for population transfer to noncomputational states, and they are present due to the weakly anharmonic and multilevel nature of the transmon. Given that these two basic ingredients are also present in the longitudinal readout circuit of Ref. [22], a natural question arises: could ionization limit the effectiveness of longitudinal readout?

In this work, we demonstrate that this is not the case. Although these deleterious multiphoton transitions are also present in the longitudinal readout, we show that they are not as prevalent as they are in dispersive readout. Crucially, they can also be mitigated by simple design choices. While previous work has focused on the transmon in the two-level approximation [22], our analysis and simulations keep the full cosine potential of the transmon [31], which was shown to be crucially important in studying ionization [17]. As discussed in more detail below, simulations accounting for the full cosine potential suggest that longitudinal readout can achieve a readout fidelity of 99.99% in less than 50 ns with realistic circuit parameters.

The rest of this manuscript is organized as follows. We first review the Hamiltonian of the circuit proposed in Ref. [22] to realize longitudinal readout, and we outline the general principles of the longitudinal transmon readout.

We then use the tools discussed in Refs. [16,17,20] to analyze the ionization properties with branch analysis and through the Schrieffer-Wolff transformation. Subsequently, we discuss the effects of the selection rules of the longitudinal readout circuit, as well as the effect of disorder in the circuit. Taking into consideration the limitations posed by ionization, we then study the performance of longitudinal readout with realistic parameters. Furthermore, we compare dispersive and longitudinal readout by treating both the transmon and the resonator classically, making remarks on the chaotic behavior of their classical descriptions [20]. Finally, we make concluding remarks.

II. LONGITUDINAL READOUT IN CQED

The circuit realizing the longitudinal interaction is composed of a flux-tunable transmon inductively coupled to a readout resonator (see Fig. 1) [22]. Intuitively, the longitudinal interaction stems from the same mechanism that allows the control of the qubit frequency of a standard flux-tunable transmon [31]. In the circuit of Fig. 1, the differential mode $\hat{\varphi}_r = (\hat{\varphi}_1 - \hat{\varphi}_2)/2$ is the resonator degree of freedom, which plays a similar role as the classical flux threading the loop of the tunable transmon. Conversely, the common mode $\hat{\varphi}_t = (\hat{\varphi}_1 + \hat{\varphi}_2)/2$ is the qubit degree of freedom. Expressed in terms of these degrees of freedom, the Hamiltonian of this circuit takes the form (see Appendix A for details)

$$\hat{H} = \omega_r \hat{a}^{\dagger} \hat{a} + 4E_C (\hat{n}_t - n_g)^2 - E_J \cos \hat{\varphi}_r \cos \hat{\varphi}_t - dE_J \sin \hat{\varphi}_r \sin \hat{\varphi}_t - i\epsilon(t) \cos (\omega_d t) (\hat{a} - \hat{a}^{\dagger}), \quad (1)$$

where we have set $\hbar = 1$ and the external flux to zero, $\varphi_{\rm ext} = 0$. In this expression, E_C is the transmon charging energy, n_g is the offset charge, and $E_J = E_{J1} + E_{J2}$ is the total Josephson energy, with $d = (E_{J2} - E_{J1})/2$ being the

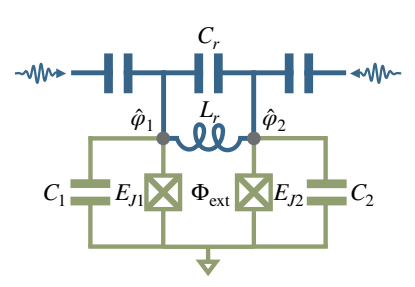


FIG. 1. Circuit diagram for longitudinal readout of a transmon qubit. A flux-tunable transmon (green) is inductively coupled to a resonator (blue). The symmetric $\hat{\varphi}_t = (\hat{\varphi}_1 + \hat{\varphi}_2)/2$ and antisymmetric $\hat{\varphi}_r = (\hat{\varphi}_1 - \hat{\varphi}_2)/2$ modes of the circuit correspond to the transmon mode and the resonator mode, respectively. The transmon and resonator modes can be driven by symmetric (inphase) and antisymmetric (out-of-phase) combinations of the two drives. In the text, we assume $C_1 = C_2$. See Appendix A for details.

junction asymmetry. The resonator mode has frequency ω_r , annihilation and creation operators \hat{a} and \hat{a}^\dagger , and flux operator $\hat{\varphi}_r = \varphi_{\rm rzpf}(\hat{a} + \hat{a}^\dagger)$, with $\varphi_{\rm rzpf} = (2\pi/\Phi_0)\sqrt{Z_r/2}$ being the resonator's zero-point phase fluctuations. Finally, ω_d is the drive frequency and $\epsilon(t)$ is the time-dependent drive amplitude.

To better highlight the transmon-resonator interaction, we use a simple trigonometric identity to write Eq. (1) as

$$\hat{H} = \omega_r \hat{a}^{\dagger} \hat{a} + \hat{H}_t - i\epsilon(t) \cos(\omega_d t) (\hat{a} - \hat{a}^{\dagger})$$

$$+ 2E_J \sin^2(\hat{\varphi}_r/2) \cos\hat{\varphi}_t - dE_J \sin\hat{\varphi}_r \sin\hat{\varphi}_t.$$
 (2)

The first line of this expression corresponds to the sum of the uncoupled, driven cavity Hamiltonian and the bare transmon Hamiltonian, $\hat{H}_t = 4E_C(\hat{n}_t - n_g)^2 - E_J \cos \hat{\varphi}_t$. The second line corresponds to two types of transmonresonator interactions. To gain an intuitive understanding of these interactions, it is useful to note that for the computational states of the transmon, $\cos \hat{\varphi}_t$ is diagonal while $\sin \hat{\varphi}_t$ is off diagonal.

As a result, when projecting in the qubit subspace, the first term of the second line gives rise to a dispersive-like interaction, whereas the second term gives rise to a transverse interaction proportional to the junction asymmetry d (see Appendix A). The impact of finite junction asymmetry will be discussed in Sec. III C, where we will show that its effects can be easily alleviated. We thus set d=0 for the moment.

Focusing on the first term of the second line of Eq. (2), we find that $\sin^2(\hat{\varphi}_r/2)$ has off-diagonal matrix elements, which can result in transitions between Fock states. Crucially, it also has diagonal matrix elements in the Fock basis, which gives rise to a dispersive interaction. Expressing the Hamiltonian in terms of its diagonal and off-diagonal components—something that can be done exactly—and projecting the transmon onto its two lowest energy levels yields (see Appendix D for details)

$$\hat{H} = [\omega_r' + \chi_z(\hat{a}^{\dagger}\hat{a})\hat{\sigma}_z]\hat{a}^{\dagger}\hat{a} + \frac{\omega_q}{2}\hat{\sigma}_z + \hat{V}(\hat{a}^2, \hat{a}^{\dagger 2})\hat{\sigma}_z$$
$$-i\epsilon(t)\cos(\omega_d t)(\hat{a} - \hat{a}^{\dagger}), \tag{3}$$

where ω_r' is the dressed resonator frequency and $\omega_q \approx \omega_p - E_C$ is the qubit frequency, in which $\omega_p = \sqrt{8E_JE_C}$ is the transmon's plasma frequency. To second order in $\varphi_{\rm rzpf}$, $\chi_z(\hat{a}^{\dagger}\hat{a}) \approx \omega_p \varphi_{\rm rzpf}^2/4$, and the first term of \hat{H} takes the form of the usual dispersive coupling. On the other hand, $\hat{V}(\hat{a}^2, \hat{a}^{\dagger 2})$ is not diagonal in the Fock basis but can only cause transitions between Fock states of the same parity. Crucially, in contrast to the dispersive readout, here, the dispersive interaction is not derived perturbatively from a parent transverse interaction. The full nonperturbative forms of $\chi_z(\hat{a}^{\dagger}\hat{a})$ and $\hat{V}(\hat{a}^2,\hat{a}^{\dagger 2})$ are indeed simply related to the matrix elements of the displacement operator in the

Fock basis [32], and their exact expressions can be found in Appendix D. Because this is not a perturbative result, the dispersive interaction strength does not scale with the inverse of the qubit-resonator detuning, as it does when it originates from a transverse interaction.

In Ref. [22], the longitudinal interaction \hat{H}_z is obtained using the circuit of Fig. 1 by modulating the external flux threading the qubit loop at the resonator frequency. Here, we use an alternative approach that, as discussed above, instead relies on driving the resonator [23]. This is made clear by moving to a displaced frame $\hat{a} \to \hat{a} + \alpha(t)$ to eliminate the drive from the Hamiltonian, where $\alpha(t)$ is determined by $\epsilon(t)$ via the linear-response properties of the resonator. Momentarily ignoring the off-diagonal contribution $\hat{V}(\hat{a}^2, \hat{a}^{\dagger 2})$ as well as the nonlinearity of the χ_z shift, in this new frame, the transformed Hamiltonian \hat{H}' takes the form [30]

$$\hat{H}' = [\omega_r + \chi_z(0)\hat{\sigma}_z]\hat{a}^{\dagger}\hat{a} + \frac{\omega_q}{2}\hat{\sigma}_z + \chi_z(0)\alpha(t)(\hat{a}^{\dagger} + \hat{a})\hat{\sigma}_z.$$
(4)

The last term of \hat{H}' has the desired longitudinal interaction of amplitude $g_z(t) = \chi_z(0)\alpha(t)$ proportional to the magnitude of the resonator displacement. At large displacement amplitudes, the longitudinal interaction overwhelms the dispersive-like interaction of amplitude $\chi_z(0)$ also present in \hat{H}' . To turn on the longitudinal interaction, below, we use a measurement drive amplitude $\epsilon(t)$ which rapidly fills the cavity with photons (see Appendix B for details on our choice of pulse shape).

This approach to obtaining a longitudinal interaction using a microwave drive rather than a flux modulation is reminiscent of the experiments reported in Refs. [33,34]. There, a longitudinal interaction is produced by driving a transversally coupled qubit with a frequency matching that of the resonator, reminiscent of the mechanism leading to the cross-resonance gate [35]. A crucial difference is that because it is based on a transverse qubit-resonator coupling, this approach is susceptible to the same non-QNDness as the dispersive readout. Moreover, for the same reason, the dispersive shift χ_x , and thus the effective longitudinal coupling $g_z \propto \chi_x$, scales inversely with the qubit-resonator detuning.

In addition to those mentioned in Sec. I, another advantage of the longitudinal readout is the lack of Jaynes-Cummings critical photon number $n_{\rm crit}^{\rm jc}=(\Delta/2g)^2$ present in the standard dispersive readout, where $\Delta=\omega_q-\omega_r$ [2]. This quantity is associated with the breakdown of the dispersive approximation. As the Hamiltonian in Eq. (4) is not derived using the dispersive approximation, there are no directly analogous quantities here. Indeed, although Eq. (4) was obtained from Eq. (2) under two approximations—projecting the Hamiltonian onto the computational

subspace and ignoring $\hat{V}(\hat{a}^2,\hat{a}^{\dagger 2})$ —these seem well justified. Within perturbation theory, any transitions we ignored are highly suppressed: the detuning between any such transitions is large, and any 2n-photon transition amplitude will be multiplied by a factor $(\varphi_{\rm rzpf}/2)^{2n} \ll 1$. It thus seems as though Eq. (4) remains valid even in the presence of strong drives. We explore this question in more detail in the next section.

III. IONIZATION IN THE LONGITUDINAL READOUT

Transmon ionization, or measurement-induced state transitions, in the dispersive readout is a consequence of photon-number-specific accidental degeneracies in the coupled qubit-resonator system [11,12,16,17,19,20]. Despite the QND character of the simplified model of Eq. (3), such degeneracies are possible in the full Hamiltonian [Eq. (2)] of the circuit of Fig. 1. In this section, we use perturbative arguments and the tools developed in Refs. [16,17] to investigate transmon ionization in longitudinal readout with the circuit of Fig. 1. More specifically, we use branch analysis to identify ionizing critical photon numbers n_{crit} and demonstrate that qubit-resonator resonances are not as detrimental as they are in dispersive readout. Moreover, we show that the critical photon numbers can be made larger simply by increasing the transmon-resonator detuning. Crucially, because of the nonperturbative nature of the cross-Kerr interaction in this circuit, this increase in detuning can be done without affecting the dispersive shift and thus the longitudinal coupling g_z . We then show that nonidealities in the longitudinal circuits, such as gate charge and junction asymmetry, do not significantly degrade its robustness to ionization.

A. Physical origin of ionization and simple mitigation strategies

To gain an intuitive understanding of the physical mechanism leading to ionization in the longitudinal readout, we begin by approximately diagonalizing the full undriven circuit Hamiltonian, Eq. (2). We first express the Hamiltonian as $\hat{H} = \hat{H}_0 + \hat{V}$, separating it into its diagonal component \hat{H}_0 and off-diagonal component \hat{V} . Without approximations, the diagonal part can be written as

$$\hat{H}_{0} = \sum_{j_{t}} \left[\omega_{r} + \chi_{z,j_{t}}(\hat{a}^{\dagger}\hat{a})|j_{t}\rangle\langle j_{t}| \right] \hat{a}^{\dagger}\hat{a}$$

$$+ \sum_{j_{t}} \left(\omega_{j_{t}} + \Lambda_{j_{t}} \right) |j_{t}\rangle\langle j_{t}|, \tag{5}$$

where ω_{j_t} are the bare transmon energies and $|j_t\rangle$ are the bare transmon states. The exact expressions for the Lamb shifts Λ_{j_t} and the nonlinear and nonperturbative dispersive shifts $\chi_{z,j_t}(\hat{a}^{\dagger}\hat{a})$ can be found in Appendix D.

The perturbation \hat{V} is then, by definition, the off-diagonal part of the interaction $2E_J \sin^2(\hat{\varphi}_r/2) \cos \hat{\varphi}_t$. Although the corresponding matrix elements can be computed exactly, to simplify the discussion, we make two approximations. We stress that these approximation are not made in the numerical results presented below. First, we treat the transmon as a Kerr nonlinear oscillator with $\hat{n}_t = -in_{\text{zpf},t}(\hat{b} - \hat{b}^{\dagger})$ and $\hat{\varphi}_t = \varphi_{\text{zpf},t}(\hat{b} + \hat{b}^{\dagger})$, where $n_{\text{zpf},t}$ and φ_{tzpf} are the zero-point fluctuations of the charge and phase, respectively [2]. Second, we only keep terms to the lowest nontrivial order in φ_{rzpf} and φ_{tzpf} , leading to [23]

$$\hat{V} pprox \left. rac{E_J \varphi_{\mathrm{rzpf}}^2}{2} (\hat{a} + \hat{a}^\dagger)^2 \left(1 - rac{\varphi_{\mathrm{tzpf}}^2}{2} (\hat{b} + \hat{b}^\dagger)^2 \right) \right|_{\mathrm{off-diag}}, \quad (6)$$

where diagonal terms such as $\hat{a}^{\dagger}\hat{a}\hat{b}^{\dagger}\hat{b}$ have already been taken into account in \hat{H}_0 . To this order in perturbation theory, \hat{V} can create or destroy pairs of excitations via terms such as $\hat{a}^{\dagger}\hat{a}(\hat{b}^2+\hat{b}^{\dagger 2})$. These processes are, however, highly off resonant, and can safely be eliminated using the standard rotating-wave approximation. The interaction \hat{V} also allows the transmon and resonator to exchange pairs of excitations via terms such as $\hat{a}^{\dagger 2}\hat{b}^2 + \hat{b}^{\dagger 2}\hat{a}^2$. Because the qubit and resonator are taken to be detuned from each other, these processes are off resonant in the absence of a drive. The nonlinear dispersive shift $\chi_{z,j_t}(\hat{a}^{\dagger}\hat{a})|j_t\rangle\langle j_t|\hat{a}^{\dagger}\hat{a}$ present in Eq. (5) can make such transitions resonant in the presence of resonator photons, and we thus expect such transitions to be the dominant factor leading to ionization. Crucially, however, these two-excitation exchange terms can be mitigated by simply increasing the qubit-cavity detuning. As a result, more photons are needed to make these unwanted processes resonant, and the onset of ionization is pushed to higher photon numbers. As explained above, this increase in the detuning can be made without sacrificing the dispersive interaction. This is in stark contrast to the dispersive readout, where the amplitude of the dispersive shift χ_x is inversely proportional to the detuning [2].

Another subtle advantage of this coupling scheme is the presence of a discrete symmetry. Indeed, formally, the full undriven Hamiltonian has a $\mathbb{Z}_2 \times \mathbb{Z}_2$ symmetry, as it is invariant under either parity transformation $\hat{\varphi}_r \to -\hat{\varphi}_r$ or $\hat{\varphi}_t \to -\hat{\varphi}_t$. While to the lowest order in perturbation theory, \hat{V} only involves pairs of excitations on either the transmon or resonator, the presence of this symmetry ensures that this conclusion is valid to all orders. This is unlike a standard transverse coupling, which only preserves the total excitation parity. This additional symmetry results in fewer pathways for the qubit and resonator to hybridize [23,36], and we thus expect our circuit to be more robust to ionization than the standard dispersive readout. Although this symmetry is broken for a finite junction asymmetry $d \neq 0$, such a term would be made negligible

by increasing the qubit-resonator detuning for the same reason as mentioned above (see Sec. III C).

From this perturbative analysis, we can thus expect that (i) the enhanced parity symmetry will prevent unwanted mixing between the transmon and resonator states, (ii) the dressed states will closely resemble the bare counterparts, at least until ionization sets in, and (iii) ionization can be pushed to higher photon numbers by increasing the resonator-transmon detuning.

B. Branch analysis

Having obtained an intuitive understanding of ionization in the longitudinal readout, we now turn to exact numerical calculations to confirm our predictions. To do so, we diagonalize the full undriven Hamiltonian Eq. (2) and use branch analysis to label the eigenstates of the composite undriven qubit-resonator system to obtain photonnumber-dependent transmon branches [16,17,37]. Each of these branches contains information about the transmon's energy levels as they vary with the number of photons in the resonator. This information can subsequently be used to understand the sudden population transfer, or ionization, of the transmon in the presence of a drive. Before doing this, we first outline the basic principle and construction of the branch analysis (see Refs. [16,17] for further details). The first step in the construction of the branches is to numerically diagonalize the full undriven Hamiltonian [Eq. (2)] in the eigenbasis $|j_t, n_r\rangle$ of the uncoupled transmon-resonator system, resulting in the set of eigenvectors $\{|\lambda\rangle\}$. For each j_t , we then find the state $|\lambda\rangle$ that maximizes the overlap $|\langle j_t, 0_r | \lambda \rangle|^2$ and label it $|\overline{j_t, 0_r}\rangle$. We then use these states $|\overline{j_t}, 0_r\rangle$ to recursively assign a label to all remaining states: $|j_t, n_r + 1\rangle$ is defined as the unassigned eigenstate $|\lambda\rangle$ that maximizes the overlap $|\langle\lambda|\hat{a}^{\dagger}|\overline{j_t},\overline{n_r}\rangle|^2$. Repeating this for each transmon index j_t results in a set of dressed states $B_{j_t} = \{|j_t, n_r\rangle\}$, which we refer to as branches.

In Fig. 2(a), we show a parametric plot of the transmon population $N_t(j_t, n_r) = \sum_{k_t, m_r} k_t |\langle k_t, m_r | j_t, n_r \rangle|^2$ of each branch as a function of the average photon number $N_r(j_t, n_r) = \langle j_t, n_r | \hat{a}^{\dagger} \hat{a} | j_t, n_r \rangle$. We see that at certain photon numbers, different branches "exchange" their transmon population, a process referred to as branch swapping [17]. Branch swapping at a given N_r results from the transmonresonator coupling in Eq. (2) and has a simple dynamical consequence: population transfer to the corresponding transmon state can occur when this number of photons is placed in the resonator. These swappings thus lead to a transition out of the computational subspace and limit the QND nature of the readout [16,17].

These branch swappings arise due to resonant multiphoton transitions between two dressed transmon states [16,17]. To illustrate this, in Fig. 2(b), we show the eigenenergies of the first 15 branches modulo the resonator

frequency ω_r . Energetic collisions between two states in this figure mean that they are resonant via some m-photon transition [11]. For each branch swapping in Fig. 2(a) there is an accompanying avoided crossing in the modular energy spectrum of Fig. 2(b). In some cases, branches cross without an avoided crossing and therefore without branch swapping. This is due to the magnitude of the transmon-resonator coupling matrix element, which scales with $\sqrt{n_r}$. At low photon numbers, these matrix elements can be too small to connect widely separated transmon states. For example, the crossing of B_{0_t} and B_{10_t} at $N_r \sim 8$ photons in Fig. 2(b) does not lead to a branch swapping in Fig. 2(a). At a larger photon number, $N_r \sim 50$, the same two branches collide again but show an anticrossing and a corresponding branch swap.

The branch analysis—which is by construction nonperturbative—confirms the validity of the intuition built using perturbation theory. For instance, unlike the standard dispersive coupling, we note that there is never any swapping between branches of different parity, a consequence of the $\mathbb{Z}_2 \times \mathbb{Z}_2$ symmetry. Consequently, there are several crossings (as opposed to avoided crossings) between branches of different parity in the modular energy spectrum. This is in stark contrast to dispersive readout, which emerges from a charge-charge coupling and therefore connects the two parity sectors of the transmon. In addition, before ionization, we see that the characters of the qubit's computational branches are largely unaffected by the presence of photons. Indeed, as we see in Fig. 2(a), the transmon populations of either branch $N_t(0_t, n_r) \approx 0$ or $N_t(1_t, n_r) \approx 1$ are approximately independent of photon number, indicating that these dressed states closely resemble their bare counterparts. Once again, this is to be contrasted with the standard dispersive readout, in which the transmon populations increase linearly with photon number, $N_t(0_t, n_r) \propto n_r$ and $N_t(1_t, n_r) \propto n_r$, a consequence of the weak transmon-resonator hybridization.

In Figs. 2(a) and 2(c), we compare the results of the branch analysis for two different qubit-resonator detunings of $\Delta/2\pi = -2.64$ and -4.34 GHz, respectively, at a constant dispersive shift $\chi_z/2\pi = -12.8$ MHz. As expected from the above discussions, the critical photon number can be made larger by increasing the qubit-resonator detuning, without affecting the value of χ_z and thus of the longitudinal coupling g_z . As discussed in more detail in Sec. IV, we stress that for a wide range of parameters, the critical photon numbers associated with ionization are well above the number of photons required to conduct fast readout. Increasing the qubit-resonator detuning is thus a valid strategy to increase the ionization threshold for a wide range of transmon parameters.

To illustrate that this conclusion applies beyond the parameters of Fig. 2, in Fig. 3(a), we plot the critical photon numbers as a function of the E_J/E_C ratio and qubit-resonator detuning $\Delta = \omega_q - \omega_r$. Here, the critical

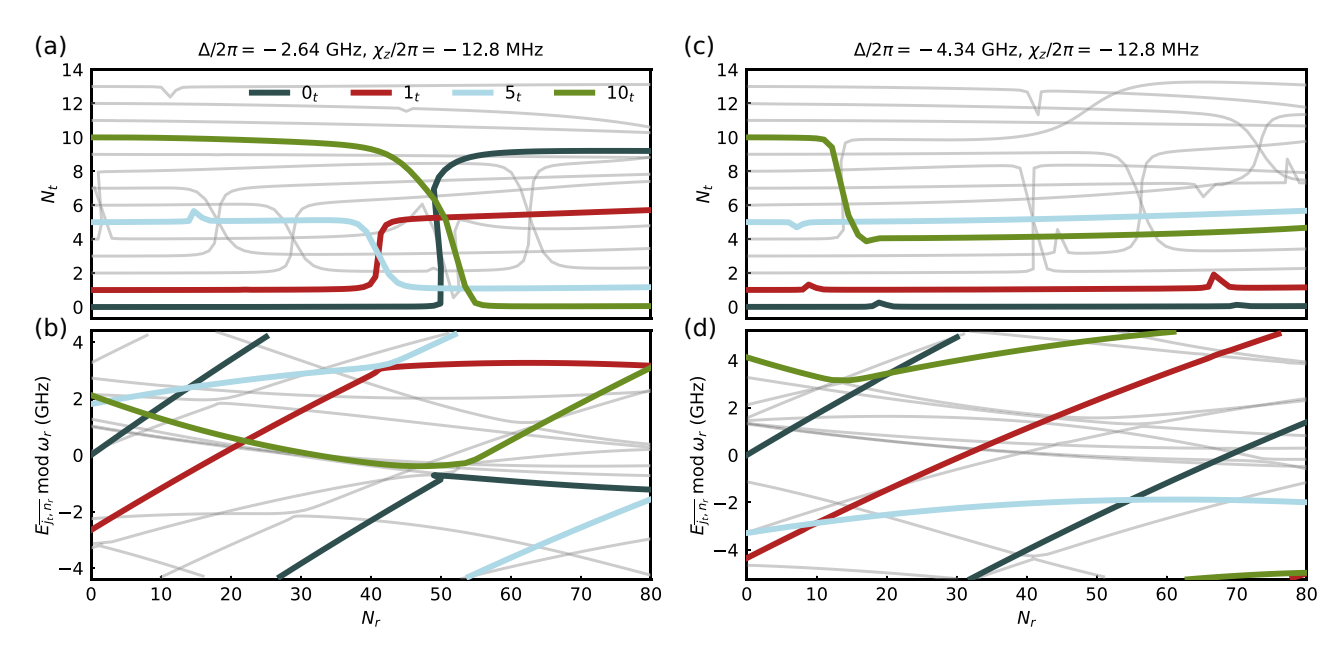


FIG. 2. (a) Transmon population as a function of the average resonator population. The ground- and excited-state branches, as well as the branches with which they swap, are highlighted. The transmon parameters are $E_C/2\pi = 0.215$ GHz, $E_J/E_C = 110$, with junction asymmetry d = 0 and gate charge $n_g = 0$. The resonator frequency is $\omega_r/2\pi = 8.8$ GHz. We keep 16 states in the transmon and 100 states in the resonator. The qubit-resonator detuning is defined as $\Delta = \omega_q - \omega_r$. (b) The energy modulo ω_r spectrum as a function of the average resonator population. Parameters are the same as in (a). The wrapping of the energies is due to the spectrum being a modulo of the resonator frequency, indicating that when two lines cross, the two states are energetically separated by an integer number of resonator photons. Avoided crossings align with branch swappings occurring in (a). (c) Transmon population as a function of average resonator population with all parameters the same as in (a) but with $\omega_r/2\pi = 10.5$ GHz. The branch swappings seen in (a) are now removed due to the higher detuning between the resonator and the transmon. (d) Energy modulo ω_r spectrum for the parameters of panel (c). Importantly, the dispersive shift χ_z is the same in (a),(c) because it is independent of detuning.

photon numbers are defined as the minimum of the critical photon numbers for the branches B_{0_t} and B_{1_t} , i.e., $n_{\text{crit}} = \min\{n_{\text{crit},0_t}, n_{\text{crit},1_t}\}$. We observe a diagonal region of low critical photon numbers beginning at $\Delta/2\pi \approx$ -2 GHz for $E_J/E_C = 50$, which persists across all E_J/E_C values, corresponding to a strong two-photon resonance between the first and fifth excited states of the transmon (see white dashed line). Indeed, this region of low critical photon number occurs due to the constant dispersive shift of the interaction, and it is dependent of how far the transmon needs to be ac-Stark shifted to cause an accidental degeneracy with a higher state. By increasing the detuning, degeneracies with the computational states can be avoided as the energy difference between the different transmon states modulo the resonator frequency increases, thus pushing the multiphoton transition further away. Indeed, the critical photon numbers increase dramatically once the detuning is increased a little past the low-critical-photonnumber region. The above phenomenon also persists when the junction asymmetry and gate charge are varied [see Figs. 3(b) and 3(c)]. Once again, the low-critical-photonnumber region is due to the same frequency collisions between the first and fifth excited states of the transmon at low photon numbers.

Finally, Fig. 3(a) illustrates that for any value of E_J/E_C , there are regions where the critical photon numbers are well above the number of photons required for a fast readout. As is expected from Fig. 2(a), if we further increase the detuning between the transmon and the resonator, the critical photon numbers increase for all values of E_J/E_C .

C. Asymmetries in the Josephson junctions and the effect of gate charge

In the above discussion, we have taken the two Josephson junctions to be identical. Realistic devices will have some amount of junction asymmetry $(d \neq 0)$ and, in that case, the last term of Eq. (2) in the two-level projection results in a transverse interaction term between the transmon and the resonator of the form $g_x(\hat{a}^\dagger + \hat{a})\hat{\sigma}_x$. This interaction lifts the selection rules suppressing ionization, allowing for more transitions to occur. While junction asymmetry should therefore be minimized in the circuit of Fig. 1, the adverse effects of this interaction can be mitigated by increasing the detuning between the transmon and the resonator. Following the discussion in the previous section, this is a second reason to work at large transmon-resonator detuning.

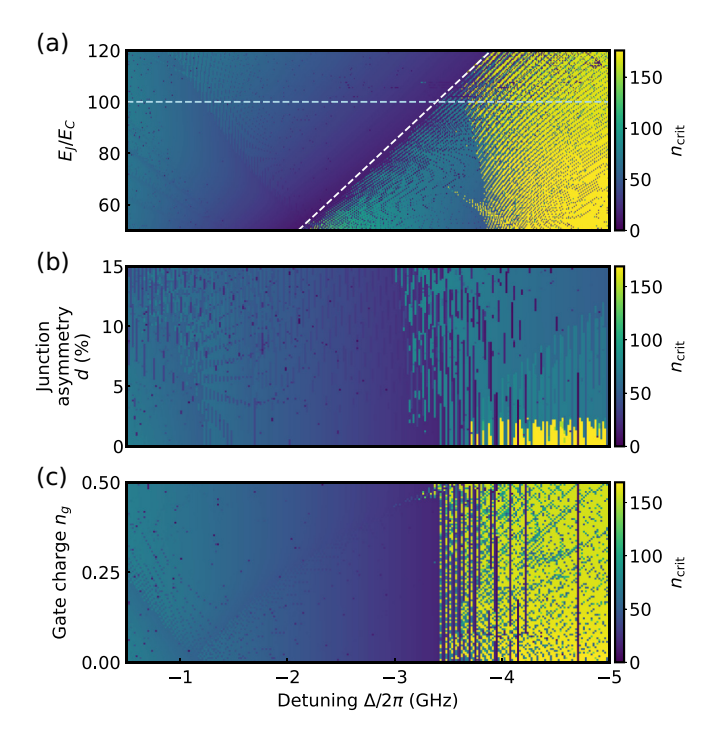


FIG. 3. (a) Critical photon numbers as a function of E_J/E_C and transmon-resonator detunings $\Delta = \omega_q - \omega_r$. The diagonal white line indicates a strong resonance between the first and the fifth excited states of the transmon that spans across all values of E_J/E_C . The blue line indicates $E_J/E_C = 100$, corresponding to the fixed E_J/E_C ratio used in panels (b),(c). (b) Ionization critical photon numbers for various detunings $\Delta/2\pi$ and Josephson-junction asymmetries d. (c) Ionization critical photon numbers as a function of detuning $\Delta/2\pi$ and gate charge n_g . For finite asymmetry and nonzero gate charge, the $\mathbb{Z}_2 \times \mathbb{Z}_2$ symmetry is broken. Despite this, we observe that the critical photon numbers, especially at high detunings, remain large. In panels (b),(c), $E_J/E_C = 100$.

Figure 3(b) shows the critical photon numbers for varying junction asymmetry up to 15%. For most detunings Δ , we observe that the critical photon numbers do not vary substantially within a few percent of asymmetry. In particular, at the higher detuning, where the critical photon numbers are high, we see a sudden drop off in the critical photon numbers; however, it is important to point out that the critical photon numbers are still high and well above the number required for a fast readout. The sensitivity to asymmetry is most apparent where the critical photon numbers are low to begin with, suggesting that the branch swappings that occur in those regions move around due to the energy shift caused by the junction asymmetry. How tolerant the parameter regime is to asymmetry will vary for the choice of E_J/E_C and the resonator frequency. It is then paramount to not only choose parameters that grant a high critical photon number in ideal conditions, but to also to choose parameters that are tolerant against some degree of imperfection.

In addition to being robust to junction disorder d, the critical photon number of the longitudinal readout depends only weakly on the transmon's gate charge n_g . This is to be contrasted with the dispersive readout, where changes in the gate charge result in large variations in the critical photon number [12,17,20]. This robustness is illustrated in Fig. 3(c), which shows the critical photon number as a function of qubit-resonator detuning and gate charge in the interval $n_g \in [0,0.5]$ for $E_J/E_C = 100$. The overall features that are observed in Fig. 3(b) are similar to what we observe in Fig. 3(a), where the critical photon numbers remain high at large detunings. In short, both nonidealities d and n_g have a small effect on the critical photon number.

IV. FAST AND HIGH-FIDELITY LONGITUDINAL READOUT

As discussed in Sec. I, under the longitudinal interaction $g_z(\hat{a}^{\dagger} + \hat{a})\hat{\sigma}_z$, the qubit-state-dependent displacement of the resonator moves at the optimal 180° out of phase from one another. Therefore, especially at shorter integration times, the signal-to-noise ratio increases more rapidly than for the dispersive readout as the pointer states separate in the optimal manner [22]. To quickly activate the longitudinal interaction and obtain a fast and high-fidelity readout, we begin by quickly displacing the resonator field to a target coherent state $|\alpha_f\rangle$, leading to a longitudinal interaction of amplitude $g_z = \alpha_f \chi_z$ [see Appendix B for the pulse shape $\varepsilon(t)$]. As an illustration, Fig. 4 shows the assignment error for different α_f , with $E_L/E_C = 50$ and $\omega_r/2\pi = 9.3$ GHz, obtained from stochastic Schrödingerequation simulations of the readout dynamics with heterodyne detection. Note that here we use $E_J/E_C = 50$ as opposed to $E_J/E_C = 100$, as in Fig. 2, as this gives a larger φ_{tzpf} and consequently a larger dispersive shift χ_z ; however, a large E_J/E_C ratio does not limit the readout performance.

Even for a moderate driving amplitude corresponding to $|\alpha_f|^2 \sim 16$ photons (light-blue line), the assignment error reaches 10^{-4} in less than 30 ns for a measurement efficiency of $\eta=1$ and in less than 50 ns for a more realistic measurement efficiency of $\eta=0.5$ (dashed light-blue line). These results are obtained for photon numbers that are well below the critical photon number, which is approximately 170 photons for the chosen parameters. See Appendix E for further details on the stochastic simulations.

Ideally, we want the fidelity and QNDness of the readout to be maximized. The two processes affecting these metrics are ionization and the resonator's self-Kerr nonlinearity. At high photon numbers, the resonator's self-Kerr nonlinearity—which, just like the dispersive shift χ_z , is nonperturbative and not controlled by the qubit-resonator detuning—can lead to "bananization" of the resonator field [38,39]. This can reduce the signal-to-noise ratio and

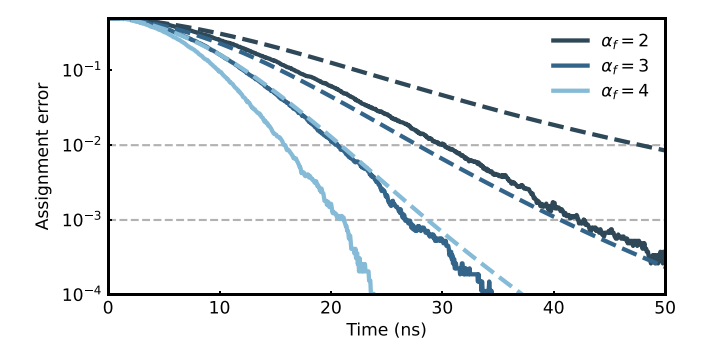


FIG. 4. Readout assignment error as a function of integration time τ for drive strengths corresponding to $\alpha_f=2,3,$ and 4. The parameters are $E_J/E_C=50,$ d=0, $n_g=0,$ $\omega_r/2\pi=9.3$ GHz, and $\kappa/2\pi=17$ MHz, and qubit relaxation is ignored. The dispersive shift is $\chi_z/2\pi\approx-8.66$ MHz, and the qubit frequency $\omega_q/2\pi\approx4.07$ GHz, corresponding to $\Delta/2\pi=-5.3$ GHz. The solid lines are results obtained from heterodyne readout simulations with the measurement efficiency set to $\eta=1$. The dashed lines are computed using the analytical expression for the signal-to-noise ratio with the efficiency set to $\eta=0.5$. See Appendices B and E for further details on the readout simulations.

thereby reduce the readout fidelity. Furthermore, a large self-Kerr nonlinearity can limit the maximum number of photons that can be placed into the resonator. Despite these possible limitations, Fig. 4, which includes these imperfections, shows that fast and high-fidelity longitudinal readout is possible.

V. EMERGENCE OF CHAOS IN THE LONGITUDINAL READOUT

In the previous sections, we have shown that the critical photon number of the longitudinal readout can be made larger than in a comparable dispersive readout, and we have argued that this robustness is linked to the symmetry of the qubit-resonator coupling in the circuit of Fig. 1. In this section, we provide another qualitative argument for the robustness of the longitudinal readout and its advantage over the dispersive readout based on the emergence of chaos in the classical model of those two readouts [20]. To do this, we follow the approach of Ref. [17], in which it was shown that the presence of classical chaos in a driven classical transmon can be linked to transmon ionization in the dispersive readout.

First, in the case of the usual dispersive readout, the classical model of the transmon is obtained from the quantum transmon-resonator Hamiltonian by neglecting the quantum fluctuations of the resonator and effectively treating the driven resonator as a classical drive on the transmon. The resulting Hamiltonian is that of a classical pendulum driven by a monochromatic drive on the pendulum's conjugate momentum [17,20,40] with the Hamiltonian

$$\tilde{H} = \frac{1}{2}\tilde{n}_t^2 - \cos\tilde{\varphi}_t + \varepsilon_t \cos(\tilde{\omega}_d \tilde{t})\tilde{n}_t. \tag{7}$$

Here, $\tilde{H}=H/E_J$, $\tilde{\varphi}_t=\varphi_t$, $\tilde{n}_t=zn_t$, and $z=\sqrt{8E_C/E_J}$ is the transmon's impedance. The phase-space coordinates satisfy the modified Poisson bracket $\{\tilde{\varphi}_t, \tilde{n}_t\} = z$. Moreover, time is rescaled to $\tilde{t}=\omega_p t$, where $\omega_p=\sqrt{8E_JE_C}$ is the plasma frequency. As a result, the renormalized drive frequency is $\tilde{\omega}_d=\omega_d/\omega_p$. Following the same approach for the longitudinal readout, we obtain the replacement $\hat{\varphi}_r\to 2\varepsilon_p\cos(\omega_d t)$ in Eq. (2), with $\varepsilon_p=\varphi_{\rm rzpf}\alpha_f$. In this expression, we have assumed the field to have reached its desired final amplitude α_f . With this replacement, neglecting quantum fluctuations of the resonator and taking d=0, Eq. (2) is transformed to

$$\tilde{H} = \frac{1}{2}\tilde{n}_t^2 - \{1 - 2\sin^2[\varepsilon_p\cos(\tilde{\omega}_d\tilde{t})]\}\cos\tilde{\varphi}_t, \quad (8)$$

corresponding to a parametrically driven pendulum [41,42].

In Figs. 5(a) and 5(c)-5(h), we present Poincaré sections obtained by plotting the phase-space coordinates at integer multiples of the drive period $\tilde{T} = 2\pi/\tilde{\omega}_d$, as obtained from solving Hamilton's equations for the dynamics governed by Eq. (8). Figure 5(a) is obtained in the absence of the parametric drive, $\varepsilon_p = 0$. In this case, all trajectories on the Poincaré section describe regular motion of the pendulum. For energy H < 1, the trajectories correspond to oscillatory motion around the minimum of energy. For a deep enough transmon—i.e., small impedance z—these are in direct correspondence with the transmon bound states [17]. Conversely, for energy $\tilde{H} > 1$, the trajectories correspond to full swings of the pendulum around its pivot point, corresponding to phase slips in the quantum model [20]. At the energy H = 1, a single trajectory—the separatrix, connecting the points $(\tilde{\varphi}_t, \tilde{n}_t) = (\pm \pi, 0)$ —defines a boundary between these two distinct types of motion [see the green line in Fig. 5(a)].

Figures 5(c), 5(e), and 5(g) show Poincaré sections for increasing drive amplitudes corresponding to $|\alpha_f|^2 \sim 1$, 9, and 49 photons, respectively. At these nonzero drive amplitudes, the aforementioned structure of the Poincaré surface is altered, and two new types of motion can emerge: (i) chaos and (ii) subharmonic resonances (see Refs. [17,20] for further details in the context of the driven transmon). The first phenomenon results from the fragility of the separatrix against integrability-breaking perturbations. In short, the branches of outgoing and ingoing motion meet at a single point $(\varphi, n) = (\pi, 0)$, and any arbitrarily weak integrability-breaking perturbation splits this arrangement, which marks the onset of an emergent chaotic region—also known as separatrix chaos (see Chapter 6 of Ref. [43]). In addition to chaotic regions, the other type of motion that emerges in the presence of the drive is subharmonic resonances, which are characterized by the appearance of islands of regular motion within the

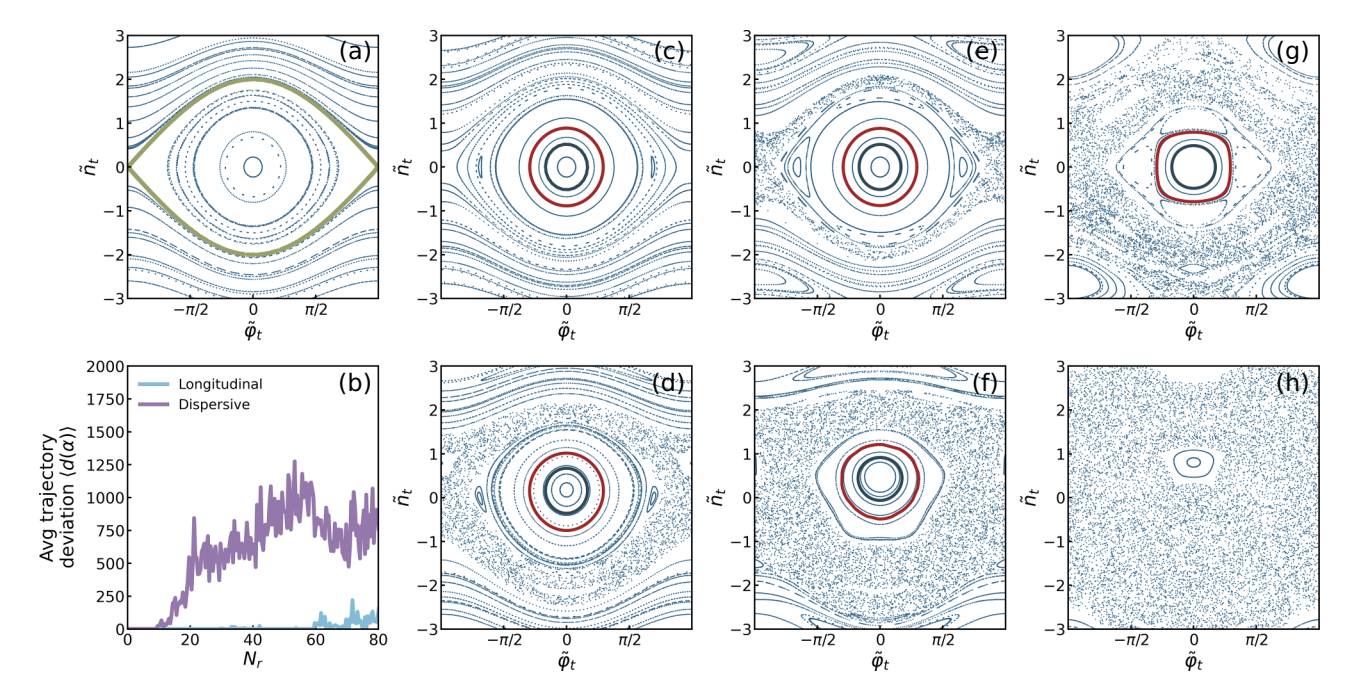


FIG. 5. (a) Poincaré section for a transmon with no drive. The green line indicates the separatrix. (b) Average trajectory deviation with increased drive amplitude. The average trajectory deviation is calculated by averaging over many trajectory deviations calculated from Eq. (9). (c),(e),(g) Poincaré sections for a transmon coupled via the longitudinal interaction with drive strengths corresponding to 1, 9, and 49 photons, respectively. The blue and red orbits indicate the Bohr-Sommerfeld orbits for the ground and first excited states of the transmon, respectively. (d),(f),(h) Poincaré sections for a transmon coupled dispersively to a resonator, again with 1, 9, and 49 photons, respectively. The blue and red orbits indicate the Bohr-Sommerfeld orbits for the ground and first excited state of the transmon, respectively. In panel (h), the regular region is too small to support a Bohr-Sommerfeld orbit. For both the longitudinal and dispersive readout cases, E_J/E_C of the transmon was set to 110. For longitudinal readout, the asymmetry was set to d = 0.

chaotic region. These are known as (n:m) nonlinear resonances and are characterized by the ratio n:m between the drive-amplitude-dependent frequency of the pendulum and the drive frequency, with n and m integers [43]. With increasing drive amplitude, the chaotic region grows and the relative importance of (n:m) resonances increases, resulting in the central regular region shrinking. As can be seen in Figs. 5(d), 5(f), and 5(h), the same phenomenology is observed for the dispersive readout (see Refs. [17,20] for detailed discussions). Crucially, however, for that readout, the chaotic region rapidly engulfs much of the phase space, dramatically impacting the regular region at its center. This is a direct consequence of the different form of the drive in the two readouts.

To understand how this phenomenology affects the qubit states, we follow Refs. [17,20] and apply the Bohr-Sommerfeld quantization rule to identify the set of initial conditions (i.e., energies) corresponding to the ground and first excited states of the transmon. This rule identifies quantized orbits for oscillatory motion as the classical orbits that enclose an area given by $A_{j_t} = 2\pi \, \hbar_{\rm eff}(j_t + 1/2)$ [44], where $j_t = 0, 1, 2, \ldots$ denotes the Bohr-Sommerfeld quantum number for the transmon state and $\hbar_{\rm eff} = z$ is the effective Planck constant [20]. The total number of Bohr-Sommerfeld states within a given area A can be calculated

as $\lfloor A/2\pi\hbar_{\rm eff} \rfloor$. The orbits corresponding to the transmon's ground and first excited states are depicted in Figs. 5(a) and 5(c)–5(h) by blue and red lines, respectively. These are regular orbits, enclosing areas $A_0 = \pi\hbar_{\rm eff}$ for the ground state and $A_1 = 3\pi\hbar_{\rm eff}$ for the first excited state. In Fig. 5(h), corresponding to a drive of 49 photons under dispersive readout, the size of the chaotic layer is such that the regular region is too small to support the regular orbits corresponding to the logical transmon states. In Refs. [17,20], this was identified as a signature of transmon ionization and linked to a critical photon number. The observation that the qubit orbits are no longer present in Fig. 5(h) for the dispersive readout is in stark contrast to the longitudinal readout where, for the same photon number, those orbits remain; compare Figs. 5(g) and 5(h).

To compare more precisely the interplay of chaos with the computational subspace in the two readout schemes, we quantify the deformation of trajectories in phase space in the presence of a drive by computing, for an initial condition $(\varphi(0), n(0))$, the deviation

$$d_{\alpha} = \sum_{t=0}^{t_{\text{max}}} \sqrt{[\varphi_0(t) - \varphi_{\alpha}(t)]^2 + [n_0(t) - n_{\alpha}(t)]^2}, \quad (9)$$

where the subscripts 0 and α indicate the classical trajectories of the undriven and driven cases with amplitude α , respectively, and t_{max} is the total evolution time. Figure 5(b) presents this quantity as a function of photon number for both dispersive (purple) and longitudinal (blue) readouts. Here, the deviation is averaged over initial conditions randomly sampled from the phase-space region spanning $[\pi h_{\text{eff}}, 4\pi h_{\text{eff}}]$. This region corresponds to the area of phase space that contains the Bohr-Sommerfeld orbits of the transmon logical subspace. As is made clear by Fig. 5 and can be intuitively understood from the Pointcaré sections of Figs. 5(c)-5(g) and 5(d)-5(h), the dispersive readout is affected to a much larger extent and at much lower photon number than the longitudinal readout. In fact, a sudden jump in the average distance is observed for the dispersive readout at approximately ten photons, while the longitudinal readout remains stable up to approximately 60 photons, and even then, only a small average distance is observed. In short, a parametrically driven transmon, corresponding to the longitudinal readout, is more robust against the emergence of chaos than a charge-driven transmon, corresponding to the dispersive readout. Interestingly, this conclusion applies to many scenarios involving parametric drives beyond longitudinal readout.

VI. CONCLUSION

We have studied the impact of multiphoton transitions in transmon longitudinal readout [22,23]. We find the threshold for ionization to be higher than for dispersive readout. Notably, this threshold can be further increased by increasing the detuning between the qubit and the resonator, and that this can be achieved without sacrificing the amplitude of the dispersive shift. We have also found the longitudinal readout to be robust against disorder in the circuit. These conclusions, obtained from a combination of numerical simulations, branch analysis, and Schrieffer-Wolff transformation, are supported by a qualitative analysis of the classical model of the transmon-resonator system. This analysis also shows that longitudinal readout, which maps to a parametrically driven nonlinear oscillator, is more robust against the onset of chaos than dispersive readout. We hope that these conclusions will motivate experimental exploration of longitudinal readout as an alternative to dispersive readout. Finally, the same tools can be used to further explore other alternative approaches to qubit readout, such as cross-Kerr readout [45], quarton-coupler-based cross-Kerr readout [46,47], and flux-qubit readout [48].

ACKNOWLEDGMENTS

The authors are grateful to Othmane Benhayoune-Khadraoui, Benjamin D'Anjou, Cristóbal Lledó, and Benjamin Groleau-Paré for helpful discussions. Support is acknowledged from NSERC, the Canada First Research Excellence Fund, the Ministère de l'Économie et de

l'Innovation du Québec, Fonds de recherche du Québec – Nature et technologies, and the U.S. Army Research Office under Grant No. W911NF-22-S-0006.

DATA AVAILABILITY

The data are available upon reasonable request from the authors.

APPENDIX A: CIRCUIT QUANTIZATION

In this section, we quantize the circuit of Fig. 1 following the standard approach of Ref. [49]. See Ref. [45] and the supplementary information of Ref. [36] for a similar analysis of the circuit. Using this approach, we find the kinetic energy of the circuit

$$K = \frac{C_1}{2}\dot{\phi}_1^2 + \frac{C_2}{2}\dot{\phi}_2^2 + \frac{C_r}{2}(\dot{\phi}_1 - \dot{\phi}_2)^2, \tag{A1}$$

and its potential energy

$$U = E_{J1}\cos\phi_1 + E_{J2}\cos\phi_2 - \frac{1}{2L_r}(\phi_1 - \phi_2 + \Phi_{\text{ext}})^2.$$
(A2)

Following the discussion in the main text, it is useful to define the two modes

$$m\phi_t = \frac{\phi_1 + \phi_2 + \Phi_{\text{ext}}}{2}, \quad \phi_r = \frac{\phi_1 - \phi_2 + \Phi_{\text{ext}}}{2}.$$
 (A3)

Substituting the above into Eqs. (A1) and (A2), we obtain the Lagrangian

$$\mathcal{L} = \frac{C_1}{2} \left(\dot{\phi}_t + \dot{\phi}_r - \dot{\Phi}_{\text{ext}} \right)^2 + \frac{C_2}{2} \left(\dot{\phi}_t - \dot{\phi}_r \right)^2 + \frac{C_r}{2} \left(2 \dot{\phi}_r - \dot{\Phi}_{\text{ext}} \right)^2 + E_{J1} \cos \left(\phi_t + \phi_r - \Phi_{\text{ext}} \right) + E_{J2} \cos \left(\phi_t - \phi_r \right) - \frac{2}{L_r} \phi_r^2.$$
(A4)

The conjugate variables q_t and q_r of the above two-mode flux are

$$q_t = \frac{\partial \mathcal{L}}{\partial \dot{\phi}_t} = C_1(\dot{\phi}_t + \dot{\phi}_r) + C_2(\dot{\phi}_t - \dot{\phi}_r), \tag{A5}$$

$$q_r = \frac{\partial \mathcal{L}}{\partial \dot{\phi}_r} = C_1(\dot{\phi}_t + \dot{\phi}_r) - C_2(\dot{\phi}_t - \dot{\phi}_r) + 4C_r\dot{\phi}_r, \quad (A6)$$

corresponding to the capacitance matrix

$$\mathbf{C} = \begin{pmatrix} C_1 + C_2 & C_1 - C_2 \\ C_1 - C_2 & C_1 + C_2 + 4C_r \end{pmatrix}. \tag{A7}$$

Assuming $C_1 = C_2 = C$, the inverted capacitance matrix is

$$\mathbf{C}^{-1} = \begin{pmatrix} \frac{1}{2C} & 0\\ 0 & \frac{1}{2C + 4C_r} \end{pmatrix}. \tag{A8}$$

In terms of the above quantities, the Hamiltonian of the system takes the general form $H = \frac{1}{2}\mathbf{q}^T\mathbf{C}^{-1}\mathbf{q} - U$, where $\mathbf{q} = (q_t, q_r)$, resulting in

$$H = \frac{q_t^2}{4C} + \frac{q_r^2}{4C + 8C_r} + \frac{2}{L_r}\phi_r^2 - E_{J1}\cos(\phi_t + \phi_r - \Phi_{\text{ext}}) - E_{J2}\cos(\phi_t - \phi_r).$$
(A9)

Promoting the two pairs of conjugate variables to operators, and introducing the charge-number operator $\hat{n}_{t,r} = \hat{q}_{t,r}/2e$, the Hamiltonian can be rewritten as

$$\hat{H} = \frac{4e^2\hat{n}_t^2}{4C} + \frac{4e^2\hat{n}_r^2}{4C + 8C_r} + \frac{2}{L}\hat{\phi}_r$$

$$-E_{J1}\cos(\hat{\phi}_t + \hat{\phi}_r - \Phi_{\text{ext}}) - E_{J2}\cos(\hat{\phi}_t - \hat{\phi}_r). \tag{A10}$$

Defining the transmon's charging energy $E_{C,r} = e^2/4C$, the resonator's charging energy $E_{C,r} = e^2/(4C + 8C_r)$, and the resonator's inductive energy $E_{L_r} = \Phi_0^2/\pi^2 L_r$, the Hamiltonian takes the form

$$\hat{H} = 4E_{C,t}\hat{n}_t^2 + 4E_{C,r}\hat{n}_r^2 + \frac{E_{L_r}}{2}\hat{\varphi}_r^2 - E_{J1}\cos(\hat{\varphi}_t + \hat{\varphi}_r - \varphi_{\text{ext}}) - E_{J2}\cos(\hat{\varphi}_t - \hat{\varphi}_r)$$
(A11)

$$= \omega_r \hat{a}^{\dagger} \hat{a} + 4E_{C,t} \hat{n}_t^2 - E_{J1} \cos{(\hat{\varphi}_t + \hat{\varphi}_r - \varphi_{\text{ext}})} - E_{J2} \cos{(\hat{\varphi}_t - \hat{\varphi}_r)}, \tag{A12}$$

where in the second line, we have introduced the resonator's creation (annihilation) operators \hat{a}^{\dagger} (\hat{a}), and $\omega_r = \sqrt{8E_{C,r}E_{L_r}}$ is the resonator frequency. We have also introduced the operators $\hat{\varphi}_{t,r} = (2\pi/\Phi_0)\hat{\phi}_{t,r}$ and $\varphi_{\rm ext} = (2\pi/\Phi_0)\phi_{\rm ext}$.

Using trigonometric identities, the last two terms of Eq. (A12) can be expressed

$$E_{J1}\cos(\hat{\varphi}_t + \hat{\varphi}_r - \varphi_{\text{ext}}) + E_{J2}\cos(\hat{\varphi}_t - \hat{\varphi}_r)$$

$$= (E_{J1}\cos\varphi_{\text{ext}} + E_{J2})\cos\hat{\varphi}_t\cos\hat{\varphi}_r$$

$$+ (E_{J2} - E_{J1}\cos\varphi_{\text{ext}})\sin\hat{\varphi}_t\sin\hat{\varphi}_r$$

$$+ E_{J1}\sin\varphi_{\text{ext}}\cos\hat{\varphi}_t\left(\sin\hat{\varphi}_r - \cos\hat{\varphi}_r\right). \tag{A13}$$

Taking the external flux to be $\varphi_{\text{ext}} = 0$, the above expression can be reduced to

$$E_J \cos \hat{\varphi}_t \cos \hat{\varphi}_r + dE_J \sin \hat{\varphi}_t \sin \hat{\varphi}_r, \qquad (A14)$$

where $E_J = E_{J1} + E_{J2}$ and $d = (E_{J2} - E_{J1})/E_J$ is the asymmetry between the Josephson-junction energies. Using these results, the Hamiltonian in Eq. (A12) can be written as

$$\hat{H} = \omega_r \hat{a}^{\dagger} \hat{a} + 4E_C \hat{n}_t^2 - E_J \cos \hat{\varphi}_t \cos \hat{\varphi}_r$$

$$- d \sin \hat{\varphi}_t \sin \hat{\varphi}_r \qquad (A15)$$

$$= \omega_r \hat{a}^{\dagger} \hat{a} + 4E_C \hat{n}_t^2 - E_J \cos \hat{\varphi}_t$$

$$+ 2E_J \cos \hat{\varphi}_t \sin^2 (\hat{\varphi}_r/2) - d \sin \hat{\varphi}_t \sin \hat{\varphi}_r, \qquad (A16)$$

where in the second line, we have again used a trigonometric identity to separate the bare transmon Hamiltonian $\hat{H}_t = 4E_C\hat{n}_t^2 - E_J\cos\hat{\varphi}_t$ from the transmon-resonator interaction, which can be read in the last line.

When including the gate charge n_g , we obtain the Hamiltonian of Eq. (2) of the main text, where we have also set $E_{C,t} = E_C$ to simplify the notation. We note that to drive the transmon (resonator) mode of this multimode circuit, the nodes labeled 1 and 2 in Fig. 1 need to be driven symmetrically (antisymmetrically); however, if there is sufficient detuning between the two modes ($\Delta = \omega_q - \omega_r$ is large), it may be possible to drive only one mode of the circuit to control both the transmon and resonator modes independently with minimal crosstalk. Once again, a large detuning is beneficial for this circuit.

To obtain a more intuitive understanding of the above Hamiltonian, Eq. (A16) can be reduced to its two-level-approximation form, which we use in the main text to relate to the dispersive-readout Hamiltonian. To obtain this reduced Hamiltonian, we first approximate the transmon Hamiltonian \hat{H}_t as $(\omega_q/2)\hat{\sigma}_z$, and we assume d=0 for simplicity. Then, using the fact that the zero-point fluctuation of the transmon and resonator is small, the interaction term $2E_J\cos\hat{\varphi}_t\sin^2(\hat{\varphi}_r/2)$ can be expanded to

$$2E_J \cos \hat{\varphi}_t \sin^2 \left(\hat{\varphi}_r/2\right)$$

$$\approx 2E_J \left(1 - \frac{\varphi_{\text{tzpf}}^2}{2} \left(\hat{b} + \hat{b}^{\dagger}\right)^2\right) \frac{\varphi_{\text{tzpf}}^2}{4} \left(\hat{a} + \hat{a}^{\dagger}\right)^2. \quad (A17)$$

Using the rotating-wave approximation and ignoring all terms that are proportional to $\hat{b}^{\dagger}\hat{b}$ and $\hat{a}^{\dagger}\hat{a}$ (which only correspond to frequency shifts of the transmon and resonator, respectively), we are left with

$$\hat{H}_{\mathrm{int}} \approx -\frac{\varphi_{\mathrm{tzpf}}^2 \varphi_{\mathrm{rzpf}}^2}{2} \hat{b}^{\dagger} \hat{b} \hat{a}^{\dagger} \hat{a}.$$
 (A18)

Using $\hat{b}^{\dagger}\hat{b}=(1/2)(1+\hat{\sigma}_z)$ and $\varphi_{\rm tzpf}=(2E_C/E_J)^{1/4}$, and setting $\chi_z=-\sqrt{2E_CE_J}\varphi_{\rm rzpf}^2/2$, we can write the two-level-approximated Hamiltonian as

$$\hat{H}_{\text{two-level}} \approx \frac{\omega_q}{2} \hat{\sigma}_z + \omega_r \hat{a}^{\dagger} \hat{a} + \chi_z \hat{\sigma}_z \hat{a}^{\dagger} \hat{a},$$
 (A19)

where we have lumped the frequency shift of the transmon (resonator) resulting from the interaction into ω_q (ω_r). Note that the above dispersive shift χ_z is not obtained with a perturbative transformation, and it depends only on the static circuit parameters such as the transmon charging and Josephson energy, as well as the phase zero-point fluctuation of the resonator (provided that $\varphi_{\rm ext}=0$). Given that the phase zero-point fluctuation of the resonator can be kept constant while changing the resonator frequency, the dispersive shift χ_z is truly independent of the detuning Δ between the qubit and the readout resonator. The benefits of breaking this trade-off between the magnitude of the dispersive shift and the detuning are highlighted in the main text, as well as below.

APPENDIX B: PULSE SHAPE

To achieve a fast turn on of the longitudinal interaction, we use a pulse shape $\epsilon(t)$ designed to rapidly fill the cavity with photons. Under the usual master equation accounting for damping of the resonator at the rate κ , the equation of motion for $\langle \hat{a} \rangle$ is

$$\langle \dot{\hat{a}} \rangle = -i\omega_r \langle \hat{a} \rangle - \frac{\kappa}{2} \langle \hat{a} \rangle + \epsilon(t) \cos(\omega_d t).$$
 (B1)

Defining $\langle \hat{a} \rangle = \alpha(t)$, we can factor the solution of the above equation to slow- and fast-oscillating terms such that $\alpha(t) = \alpha_p(t)e^{-i\omega_r t}$. Substituting this into the above equation, and applying the rotating-wave approximation, we get

$$\dot{\alpha}_p(t) = -\frac{\kappa}{2}\alpha_f(t) + \frac{\epsilon(t)}{2}.$$
 (B2)

Using this expression, we choose a desired $\alpha_p(t)$ and obtain the corresponding form of $\epsilon(t)$. Here, we take $\alpha_p(t) = \alpha_f(1 - \exp(-(t/\tau)^2))$, where α_f is the amplitude of the target coherent state. From Eq. (B2), we can then express the pulse as

$$\epsilon(t) = \frac{4t\alpha_f}{\tau^2} e^{-(t/\tau)^2} + \kappa \alpha_f (1 - e^{-(t/\tau)^2}).$$
 (B3)

The above pulse is designed to quickly displace the resonator to a coherent state with an amplitude α_f and maintain it by accounting for dissipation. The speed at which the displacement is made is controlled by adjusting τ . The pulse shapes used in Fig. 4 are shown in Fig. 6. For $\alpha_f = 4$,

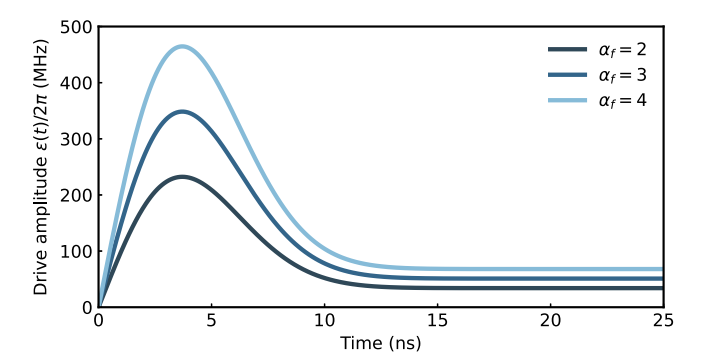


FIG. 6. Pulses used for the readout simulations in Fig. 4, shown up to t = 25 ns. Here, $\tau = 5$ and $\kappa/2\pi = 17$ MHz.

the maximum drive amplitude is $\varepsilon_{\rm max}/2\pi \approx 465$ MHz, and this is reached in approximately 5 ns.

It is important to point out that the phase of the drive must be constant to activate the longitudinal interaction most effectively. Aside from experimental limitations, there are no restrictions on the pulse shape, and it could be interesting to consider whether more sophisticated pulses could further improve performance, just like in dispersive readout [5,50].

APPENDIX C: IDENTIFICATION OF CRITICAL PHOTON NUMBER

We identify the critical photon number for ionization of the ground (excited) state of the transmon from the branch analysis as the number of photons in the resonator that is required for the transmon population to exceed $N_t = 2$ ($N_t = 3$) for at least three consecutive photons (see Ref. [17] for details). The last condition is to avoid identifying small resonances that can bring the population over the threshold at a single resonator photon number. See, for example, the small population jump due to a small resonance between states 1_t and 5_t in Fig. 2(c).

APPENDIX D: SCHRIEFFER-WOLFF TRANSFORMATION

In this section, we derive the Schrieffer-Wolff transformation for the longitudinal-readout Hamiltonian, Eq. (2), assuming d=0 and in the absence of a drive. We express this Hamiltonian as

$$\hat{H} = \hat{H}_0' + \hat{V}',\tag{D1}$$

with

$$\hat{H}'_0 = \omega_r \hat{a}^{\dagger} \hat{a} + \sum_{j_t} \omega_{j_t} |j_t\rangle \langle j_t|$$
 (D2)

and

$$\hat{V}' = 2E_J \cos \hat{\varphi}_t \sin^2 (\hat{\varphi}_r/2), \tag{D3}$$

where $|j_t\rangle$ are the transmon eigenstates and ω_{j_t} are the corresponding energies. Note that \hat{V}' has diagonal components

in the basis in which we have expressed \hat{H}'_0 . We separate out this diagonal contribution, from which we define \hat{H}_0 in the main text. The off-diagonal parts are then, by definition, \hat{V} . Using the trigonometric identity $2\sin^2\theta/2 = 1 - \cos\theta$, we can express \hat{V}' as a sum of displacement operators $\hat{D}(\alpha)$:

$$\cos \hat{\varphi}_r = \frac{1}{2} \left(e^{i\varphi_{\text{rzpf}}(\hat{a} + \hat{a}^{\dagger})} + e^{-i\varphi_{\text{rzpf}}(\hat{a} + \hat{a}^{\dagger})} \right)$$
$$= \frac{1}{2} \left[D(i\varphi_{\text{rzpf}}) + D(-i\varphi_{\text{rzpf}}) \right]. \tag{D4}$$

The matrix elements of the displacement operator in the Fock basis are well known and take the form [32]

$$\langle n_r | D(\alpha) | m_r \rangle = \sqrt{\frac{m_r!}{n_r!}} \alpha^{n_r - m_r} e^{-|\alpha|^2/2} L_{m_r}^{n_r - m_r} (|\alpha|^2), \quad (D5)$$

where $n_r \ge m_r$ and L_a^b is the generalized Laguerre polynomial (in which a is a nonnegative integer and b is a real number), we can write the interaction term as

$$\hat{V}' = E_J \sum_{i_t,j_t} \langle i_t | \cos \hat{\varphi}_t | j_t \rangle |i_t \rangle \langle j_t |
- \frac{E_J}{2} e^{-\varphi_{\text{rzpf}}^2/2} \sum_{i_t,i_t} \sum_{n_t,m_r} \langle i_t | \cos \hat{\varphi}_t | j_t \rangle \sqrt{\frac{m_r!}{n_r!}} (i\varphi_{\text{rzpf}})^{n_r - m_r} L_{m_r}^{n_r - m_r} (\varphi_{\text{rzpf}}^2) \left[1 + (-1)^{n_r - m_r} \right] |i_t, n_r \rangle \langle j_t, m_r| .$$
(D6)

The total Hamiltonian can then be written as in the main text,

$$\hat{H} = \hat{H}'_0 + \hat{V}' = \hat{H}_0 + \hat{V},\tag{D7}$$

with

$$\hat{H}_{0} = \omega_{r} \hat{a}^{\dagger} \hat{a} + \sum_{j_{t}} \left(\omega_{j_{t}} + E_{J} \langle j_{t} | \cos \hat{\varphi}_{t} | j \rangle \right) |j_{t} \rangle \langle j_{t}| - E_{J} e^{-\varphi_{\text{rzpf}}^{2}/2} \sum_{j_{t}} \sum_{m_{r}} \langle j_{t} | \cos \hat{\varphi}_{t} | j_{t} \rangle L_{m_{r}} (\varphi_{\text{rzpf}}^{2}) |j_{t}, m_{r} \rangle \langle j_{t}, m_{r}|$$

$$= \sum_{j_{t}} \left[\omega_{r} + \chi_{z,j_{t}} (\hat{a}^{\dagger} \hat{a}) |j_{t} \rangle \langle j_{t}| \right] \hat{a}^{\dagger} \hat{a} + \sum_{j_{t}} \left(\omega_{j_{t}} + \Lambda_{j_{t}} \right) |j_{t} \rangle \langle j_{t}|,$$
(D8)

where

$$\hat{a}^{\dagger}\hat{a}\chi_{z,j_t}(\hat{a}^{\dagger}\hat{a}) = -E_J e^{-\varphi_{\text{rzpf}}^2/2} L_{\hat{a}^{\dagger}\hat{a}}(\varphi_{\text{rzpf}}^2) \sum_{i_t} \langle j_t | \cos \hat{\varphi}_t | j_t \rangle \tag{D9}$$

is the transmon-dependent shift to the resonator frequency and

$$\Lambda_{i_t} = E_J \langle j_t | \cos \hat{\varphi}_t | j_t \rangle \tag{D10}$$

is a resonator-independent shift of the transmon's frequency. Moreover, the off-diagonal part of the interaction term can then be written as

$$\hat{V} = E_{J} \sum_{i_{t} \neq j_{t}} \langle i_{t} | \cos \hat{\varphi}_{t} | j_{t} \rangle | i_{t} \rangle \langle j_{t} |
- \frac{E_{J}}{2} e^{-\varphi_{\text{rzpf}}^{2}/2} \sum_{(i_{t}, n_{r}) \neq (j_{t}, m_{r})} \langle i_{t} | \cos \hat{\varphi}_{t} | j_{t} \rangle \sqrt{\frac{m_{r}!}{n_{r}!}} (i\varphi_{\text{rzpf}})^{n_{r} - m_{r}} L_{m_{r}}^{n_{r} - m_{r}} (\varphi_{\text{rzpf}}^{2}) \left[1 + (-1)^{n_{r} - m_{r}} \right] |i_{t}, n_{r} \rangle \langle j_{t}, m_{r}|.$$
(D11)

Having separated out the diagonal and off-diagonal contributions, we now perform a Schrieffer-Wolff transformation on Eq. (D7) to eliminate the off-diagonal contribution to second order to obtain the effective Hamiltonian

$$e^{\hat{S}}\hat{H}e^{-\hat{S}} \approx \hat{H}_0 + \hat{H}^{(2)} + \dots,$$
 (D12)

where \hat{S} is the Schrieffer-Wolff transformation generator and

$$\hat{H}^{(2)} = \sum_{i_t, i_r, k_t} \sum_{n_r, m_r, l_r} \frac{1}{2} \eta_{i_t, k_t, n_r, l_r} \eta_{k_t, j_t, l_r, m_r} \left(\frac{1}{\omega_{i_t, k_t} + (n_r - l_r)\omega_r'} + \frac{1}{\omega_{j_t, k_t} + (m_r - l_r)\omega_r'} \right) |i_t, n_r\rangle\langle j_t, m_r|, \tag{D13}$$

with $\omega_{a_t,b_t} = \omega_{a_t} - \omega_{b_t}$, where ω_{a_t} and ω_{b_t} are the ac-Stark-shifted transmon frequencies, ω_r' is the resonator frequency shifted by $\chi_{z,j_t}(\hat{a}^{\dagger}\hat{a})$, and the matrix elements η_{a_t,b_t,c_r,d_r} are given by

$$\eta_{a_{l},b_{l},c_{r},d_{r}} = E_{J} \langle a_{t} | \cos \hat{\varphi}_{t} | b_{t} \rangle \delta_{c_{r},d_{r}} \\
- \frac{E_{J}}{2} e^{-\varphi_{\text{rzpf}}^{2}/2} \langle a_{t} | \cos \hat{\varphi}_{t} | b_{t} \rangle \sqrt{\frac{d_{r}!}{c_{r}!}} (i\varphi_{\text{rzpf}})^{c_{r}-d_{r}} L_{d_{r}}^{c_{r}-d_{r}} (\varphi_{\text{rzpf}}^{2}) \left[1 + (-1)^{c_{r}-d_{r}} \right]. \tag{D14}$$

It is worth noting that the selection rules for both the transmon and the resonator are now apparent. As mentioned in the main text, the cosine function is even and, therefore, only states with the same parity can be connected with matrix elements $\langle i_t | \cos \hat{\varphi}_t | j_t \rangle$. We observe similar selection rules for the resonator. This can be seen in Eq. (D6), where the term $[1 + (-1)^{n_r - m_r}]$ only connects resonator states if $n_r - m_r$ is even. These selection rules are beneficial for the readout as they prevent unwanted transitions between the computational states and reduce the number of pathways through which transitions to higher states can occur.

Furthermore, the diagonal Hamiltonian of Eq. (D8) includes the Lamb shift, as well as the cross-Kerr coupling that is used for the readout. As mentioned in the main text, an important point is that the cross-Kerr coupling does not depend on the transmon-resonator detuning. Moreover, the off-diagonal terms that lead to ionization are in Eq. (D13). Crucially, unlike the cross-Kerr coupling, however, these terms *do* depend on the detuning between the transmon and the resonator. Therefore, increasing the detuning can then suppress the terms that lead to ionization.

APPENDIX E: READOUT SIMULATIONS

To model the readout and obtain an accurate estimation of the assignment error, we numerically model a single-shot readout measurement with heterodyne detection using QUTIP's stochastic Schrödinger-equation solver [51,52]. The stochastic Schrödinger equation we are solving is

$$d\psi(t) = -i\hat{H}\psi(t)dt - \left(\frac{\kappa}{2}\hat{a}^{\dagger}\hat{a} - \frac{\kappa}{4}[\langle\hat{x}\rangle + i\langle\hat{p}\rangle]\hat{a}\right) + \frac{\kappa}{16}[\langle\hat{x}\rangle^2 + \langle\hat{p}\rangle^2]\psi(t) + \sqrt{\frac{\kappa}{2}}\left(\hat{a} - \frac{\langle\hat{x}\rangle}{2}\right)\psi(t)dW_x - \sqrt{\frac{\kappa}{2}}\left(i\hat{a} + \frac{\langle\hat{p}\rangle}{2}\right)\psi(t)dW_p.$$
 (E1)

Here, \hat{H} is the Hamiltonian from Eq. (1), κ is the resonator decay rate, and $\hat{x} = \hat{a} + \hat{a}^{\dagger}$ and $\hat{p} = i(\hat{a}^{\dagger} - \hat{a})$ are the measured quadratures. Both measured quadratures have independent Wiener increments dW_i that satisfy $\mathbb{E}[dW_i] = 0$ and $\mathbb{E}[dW_idW_j] = \delta_{ij}dt$, where $i,j \in \{x,p\}$. For each trajectory, we demodulate the signal with $e^{i\omega_d t}$ and integrate the signal from both the x and p quadratures using the real and imaginary parts of the optimal weighting function $\langle a_e(t) \rangle - \langle a_g(t) \rangle$, respectively [53].

By simulating multiple trajectories, with the qubit initialized in the ground or excited state, we obtain two clusters of points in the IQ plane as a function of time. At each time step t, we find the optimal threshold line that separates the two clusters of points, which results in the minimal assignment error $\varepsilon(t)$, computed as

$$\varepsilon(t) = \frac{P(e|g)(t) + P(g|e)(t)}{2},\tag{E2}$$

where P(x|y)(t) is the conditional probability of assigning the readout outcome as x when starting in the yth state. In our simulations, we use a step size of π/ω_d , with nsubsteps set to 6000 for a target coherent-state amplitude of $\alpha_f=2$, and to 10 000 for $\alpha_f=3$ and 4. We simulated 81 920, 26 624, and 27 648 trajectories for the target coherent-state amplitudes $\alpha_f=2$, 3, and 4, respectively. For the stochastic readout simulations, we do not average over gate charges; however, as indicated in Fig. 7, we find that the critical photon number does not dip below $n_{\text{max}}=16$, the maximum number of photons we put in the resonator in our simulations.

Computing the assignment fidelity in the above way accounts for any non-Gaussian effects in the phase space that may be overlooked when using analytical expressions that assume the resonator fields as coherent states; however, given the relatively low self-Kerr nonlinearity on the resonator (approximately 340 kHz), we find that the non-Gaussian effects on the resonator fields are minimal at the photon numbers used in our readout simulations. We can

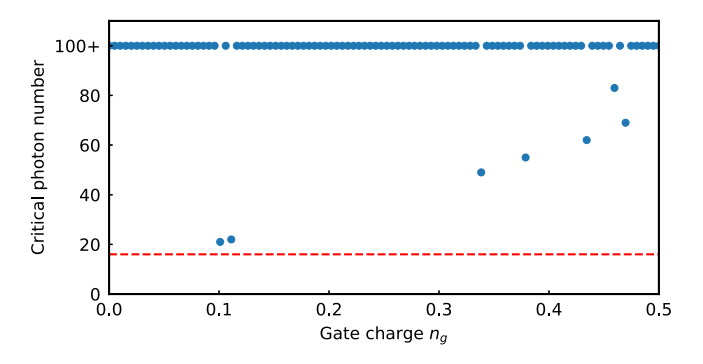


FIG. 7. Critical photon number for the parameters used in the stochastic readout simulations for Fig. 4 as a function of varying gate charge n_g . The red line indicates the maximum number of photons n_{max} that we put in the resonator for the readout simulations. For all gate charges scanned, the critical photon number remains above n_{max} .

then approximate the resonator states to be coherent states and compute the optimal signal-to-noise ratio with

$$SNR(t_m) = \sqrt{2\kappa\eta \int_0^{t_m} |\alpha_e(t) - \alpha_g(t)|^2 dt},$$
 (E3)

where η is the measurement efficiency, t_m is the integration time, and $\alpha_g(t)$ ($\alpha_e(t)$) is the resonator mean field when the qubit is prepared in the ground (excited) state. We compute the resonator mean field using QUTIP's Monte Carlo solver with 500 trajectories. The assignment fidelity can then be computed with

$$\varepsilon(t_m) = \frac{1}{2} \operatorname{erfc}\left(\frac{\operatorname{SNR}(t_m)}{2\sqrt{2}}\right),$$
 (E4)

where erfc is the complementary error function. The estimated assignment errors with the measurement efficiency set to $\eta = 0.5$ are shown in Fig. 4.

- [1] B. M. Terhal, Quantum error correction for quantum memories, Rev. Mod. Phys. **87**, 307 (2015).
- [2] A. Blais, A. L. Grimsmo, S. M. Girvin, and A. Wallraff, Circuit quantum electrodynamics, Rev. Mod. Phys. 93, 025005 (2021).
- [3] P. A. Spring, L. Milanovic, Y. Sunada, S. Wang, A. F. van Loo, S. Tamate, and Y. Nakamura, Fast multiplexed superconducting-qubit readout with intrinsic Purcell filtering using a multiconductor transmission line, PRX Quantum 6, 020345 (2025).
- [4] F. Swiadek, R. Shillito, P. Magnard, A. Remm, C. Hellings, N. Lacroix, Q. Ficheux, D. C. Zanuz, G. J. Norris, A. Blais, S. Krinner, and A. Wallraff, Enhancing dispersive readout of superconducting qubits through dynamic control of the dispersive shift: Experiment and theory, PRX Quantum 5, 040326 (2024).

- [5] T. Walter, P. Kurpiers, S. Gasparinetti, P. Magnard, A. Potočnik, Y. Salathé, M. Pechal, M. Mondal, M. Oppliger, C. Eichler, and A. Wallraff, Rapid high-fidelity single-shot dispersive readout of superconducting qubits, Phys. Rev. Appl. 7, 054020 (2017).
- [6] Y. Sunada, S. Kono, J. Ilves, S. Tamate, T. Sugiyama, Y. Tabuchi, and Y. Nakamura, Fast readout and reset of a superconducting qubit coupled to a resonator with an intrinsic Purcell filter, Phys. Rev. Appl. 17, 044016 (2022).
- [7] Z. Li, P. Liu, P. Zhao, Z. Mi, H. Xu, X. Liang, T. Su, W. Sun, G. Xue, J.-N. Zhang, W. Liu, Y. Jin, and H. Yu, Error per single-qubit gate below 10⁻⁴ in a superconducting qubit, npj Quantum Inf. 9, 111 (2023).
- [8] R. Li, K. Kubo, Y. Ho, Z. Yan, Y. Nakamura, and H. Goto, Realization of high-fidelity CZ gate based on a double-transmon coupler, Phys. Rev. X 14, 041050 (2024).
- [9] Y. Sung, L. Ding, J. Braumüller, A. Vepsäläinen, B. Kannan, M. Kjaergaard, A. Greene, G. O. Samach, C. McNally, D. Kim, A. Melville, B. M. Niedzielski, M. E. Schwartz, J. L. Yoder, T. P. Orlando, S. Gustavsson, and W. D. Oliver, Realization of high-fidelity CZ and ZZ-free iSWAP gates with a tunable coupler, Phys. Rev. X 11, 021058 (2021).
- [10] A. Somoroff, Q. Ficheux, R. A. Mencia, H. Xiong, R. Kuzmin, and V. E. Manucharyan, Millisecond coherence in a superconducting qubit, Phys. Rev. Lett. 130, 267001 (2023).
- [11] D. Sank *et al.*, Measurement-induced state transitions in a superconducting qubit: Beyond the rotating wave approximation, Phys. Rev. Lett. **117**, 190503 (2016).
- [12] M. Khezri, A. Opremcak, Z. Chen, K. C. Miao, M. McEwen, A. Bengtsson, T. White, O. Naaman, D. Sank, A. N. Korotkov, Y. Chen, and V. Smelyanskiy, Measurement-induced state transitions in a superconducting qubit: Within the rotating-wave approximation, Phys. Rev. Appl. 20, 054008 (2023).
- [13] Z. K. Minev, S. O. Mundhada, S. Shankar, P. Reinhold, R. Gutiérrez-Jáuregui, R. J. Schoelkopf, M. Mirrahimi, H. J. Carmichael, and M. H. Devoret, To catch and reverse a quantum jump mid-flight, Nature 570, 200 (2019).
- [14] R. Lescanne, L. Verney, Q. Ficheux, M. H. Devoret, B. Huard, M. Mirrahimi, and Z. Leghtas, Escape of a driven quantum Josephson circuit into unconfined states, Phys. Rev. Appl. 11, 014030 (2019).
- [15] T. Thorbeck, Z. Xiao, A. Kamal, and L. C. G. Govia, Readout-induced suppression and enhancement of superconducting qubit lifetimes, Phys. Rev. Lett. 132, 090602 (2024).
- [16] R. Shillito, A. Petrescu, J. Cohen, J. Beall, M. Hauru, M. Ganahl, A. G. Lewis, G. Vidal, and A. Blais, Dynamics of transmon ionization, Phys. Rev. Appl. 18, 034031 (2022).
- [17] M. F. Dumas, B. Groleau-Paré, A. McDonald, M. H. Muñoz Arias, C. Lledó, B. D'Anjou, and A. Blais, Measurementinduced transmon ionization, Phys. Rev. X 14, 041023 (2024).
- [18] L. Verney, R. Lescanne, M. H. Devoret, Z. Leghtas, and M. Mirrahimi, Structural instability of driven Josephson circuits prevented by an inductive shunt, Phys. Rev. Appl. 11, 024003 (2019).
- [19] X. Xiao, J. Venkatraman, R. G. Cortiñas, S. Chowdhury, and M. H. Devoret, A diagrammatic method to compute

- the effective Hamiltonian of driven nonlinear oscillators, arXiv:2304.13656 [quant-ph].
- [20] J. Cohen, A. Petrescu, R. Shillito, and A. Blais, Reminiscence of classical chaos in driven transmons, PRX Quantum 4, 020312 (2023).
- [21] J. Gambetta, A. Blais, M. Boissonneault, A. A. Houck, D. I. Schuster, and S. M. Girvin, Quantum trajectory approach to circuit QED: Quantum jumps and the Zeno effect, Phys. Rev. A 77, 012112 (2008).
- [22] N. Didier, J. Bourassa, and A. Blais, Fast quantum nondemolition readout by parametric modulation of longitudinal qubit-oscillator interaction, Phys. Rev. Lett. 115, 203601 (2015).
- [23] M. Lachapelle, Mesure optimale des qubits supraconducteurs, Master's thesis, Université de Sherbrooke, 2018.
- [24] S. Richer, N. Maleeva, S. T. Skacel, I. M. Pop, and D. DiVincenzo, Inductively shunted transmon qubit with tunable transverse and longitudinal coupling, Phys. Rev. B 96, 174520 (2017).
- [25] A. J. Kerman, Quantum information processing using quasiclassical electromagnetic interactions between qubits and electrical resonators, New J. Phys. 15, 123011 (2013).
- [26] P.-M. Billangeon, J. S. Tsai, and Y. Nakamura, Circuit-QED-based scalable architectures for quantum information processing with superconducting qubits, Phys. Rev. B 91, 094517 (2015).
- [27] C. A. Potts, R. C. Dekker, S. Deve, E. W. Strijbis, and G. A. Steele, Strong intrinsic longitudinal coupling in circuit quantum electrodynamics, Phys. Rev. Lett. **134**, 153603 (2025).
- [28] K. V. Salunkhe, S. Kundu, S. Das, J. Deshmukh, M. P. Patankar, and R. Vijay, The quantromon: A qubitresonator system with orthogonal qubit and readout modes, arXiv:2501.17439 [quant-ph].
- [29] M. H. Muñoz Arias, C. Lledó, and A. Blais, Qubit readout enabled by qubit cloaking, Phys. Rev. Appl. 20, 054013 (2023).
- [30] A. Blais, J. Gambetta, A. Wallraff, D. I. Schuster, S. M. Girvin, M. H. Devoret, and R. J. Schoelkopf, Quantum-information processing with circuit quantum electrodynamics, Phys. Rev. A 75, 032329 (2007).
- [31] J. Koch, T. M. Yu, J. Gambetta, A. A. Houck, D. I. Schuster, J. Majer, A. Blais, M. H. Devoret, S. M. Girvin, and R. J. Schoelkopf, Charge-insensitive qubit design derived from the Cooper pair box, Phys. Rev. A 76, 042319 (2007).
- [32] K. E. Cahill and R. J. Glauber, Ordered expansions in Boson amplitude operators, Phys. Rev. 177, 1857 (1969).
- [33] S. Touzard, A. Kou, N. E. Frattini, V. V. Sivak, S. Puri, A. Grimm, L. Frunzio, S. Shankar, and M. H. Devoret, Gated conditional displacement readout of superconducting qubits, Phys. Rev. Lett. 122, 080502 (2019).
- [34] J. Ikonen, J. Goetz, J. Ilves, A. Keränen, A. M. Gunyho, M. Partanen, K. Y. Tan, D. Hazra, L. Grönberg, V. Vesterinen, S. Simbierowicz, J. Hassel, and M. Möttönen, Qubit measurement by multichannel driving, Phys. Rev. Lett. 122, 080503 (2019).
- [35] J. M. Chow, A. D. Córcoles, J. M. Gambetta, C. Rigetti, B. R. Johnson, J. A. Smolin, J. R. Rozen, G. A. Keefe, M. B. Rothwell, M. B. Ketchen, and M. Steffen, Simple all-microwave entangling gate for fixed-frequency superconducting qubits, Phys. Rev. Lett. 107, 080502 (2011).

- [36] Y. Lu, A. Maiti, J. W. O. Garmon, S. Ganjam, Y. Zhang, J. Claes, L. Frunzio, S. M. Girvin, and R. J. Schoelkopf, High-fidelity parametric beamsplitting with a parity-protected converter, Nat. Commun. 14, 5767 (2023).
- [37] M. Boissonneault, J. M. Gambetta, and A. Blais, Improved superconducting qubit readout by qubit-induced nonlinearities, Phys. Rev. Lett. 105, 100504 (2010).
- [38] V. Sivak, N. Frattini, V. Joshi, A. Lingenfelter, S. Shankar, and M. Devoret, Kerr-free three-wave mixing in superconducting quantum circuits, Phys. Rev. Appl. 11, 054060 (2019).
- [39] S. Boutin, D. M. Toyli, A. V. Venkatramani, A. W. Eddins, I. Siddiqi, and A. Blais, Effect of higher-order nonlinearities on amplification and squeezing in Josephson parametric amplifiers, Phys. Rev. Appl. **8**, 054030 (2017).
- [40] R. Graham and J. Keymer, Level repulsion in power spectra of chaotic Josephson junctions, Phys. Rev. A 44, 6281 (1991).
- [41] J. B. McLaughlin, Period-doubling bifurcations and chaotic motion for a parametrically forced pendulum, J. Stat. Phys. 24, 375 (1981).
- [42] S. P. Hastings and J. B. McLeod, Chaotic motion of a pendulum with oscillatory forcing, Am. Math. Mon. 100, 563 (1993).
- [43] G. Zaslavsky, *Hamiltonian Chaos and Fractional Dynamics* (OUP, Oxford, 2005).
- [44] A. Messiah, Quantum Mechanics (Dover Publications, Inc., Garden City, New York, 2020).
- [45] R. Dassonneville, T. Ramos, V. Milchakov, L. Planat, E. Dumur, F. Foroughi, J. Puertas, S. Leger, K. Bharadwaj, J. Delaforce, C. Naud, W. Hasch-Guichard, J. J. García-Ripoll, N. Roch, and O. Buisson, Fast high-fidelity quantum nondemolition qubit readout via a nonperturbative cross-Kerr coupling, Phys. Rev. X 10, 011045 (2020).
- [46] Y. Ye, J. B. Kline, S. Chen, A. Yen, and K. P. O'Brien, Ultrafast superconducting qubit readout with the quarton coupler, Sci. Adv. 10, eado9094 (2024).
- [47] Y. Ye, K. Peng, M. Naghiloo, G. Cunningham, and K. P. O'Brien, Engineering purely nonlinear coupling between superconducting qubits using a quarton, Phys. Rev. Lett. **127**, 050502 (2021).
- [48] X. Wang, A. Miranowicz, and F. Nori, Ideal quantum nondemolition readout of a flux qubit without Purcell limitations, Phys. Rev. Appl. **12**, 064037 (2019).
- [49] U. Vool and M. Devoret, Introduction to quantum electromagnetic circuits, Int. J. Circuit Theory Appl. 45, 897 (2017).
- [50] R. Gautier, Élie Genois, and A. Blais, Optimal control in large open quantum systems: The case of transmon readout and reset, Phys. Rev. Lett. 134, 070802 (2025).
- [51] J. Johansson, P. Nation, and F. Nori, QuTiP: An opensource Python framework for the dynamics of open quantum systems, Comput. Phys. Commun. 183, 1760 (2012).
- [52] J. Johansson, P. Nation, and F. Nori, QuTiP 2: A Python framework for the dynamics of open quantum systems, Comput. Phys. Commun. 184, 1234 (2013).
- [53] C. C. Bultink, B. Tarasinski, N. Haandbæk, S. Poletto, N. Haider, D. J. Michalak, A. Bruno, and L. DiCarlo, General method for extracting the quantum efficiency of dispersive qubit readout in circuit QED, Appl. Phys. Lett. 112, 092601 (2018).